Device Design for Multitask Graphene Electromagnetic Detection Based on Second Harmonic Generation

Cheng Yang, Chu-Ming Guo, Jie Xu, and Hai-Feng Zhang

***Abstract*— The generation of a second harmonic wave (SHW) is a process of electromagnetic radiation at a specific frequency, often occurring in polarized ferroelectric crystals (FCs). In this article, a multitask graphene electromagnetic detection device (GEDD) based on second harmonic generation (SHG) is proposed. Through the periodic arrangement of different dielectric materials, the SHW conversion efficiency steadily increases within the structure, enabling multiscale detection of graphene thickness, angle, and hemoglobin concentration. By utilizing the shift f_1 in the SHW peak (SHWP), the number of graphene layers (ranging from one to ten layers) can be accurately identified through thickness detection. The sensitivity (S) is 62.1 GHz/nm. Leveraging the high-S of 147 GHz/°, the shift f_2 in the SHWP within the graphene structure can be employed for precise small-angle detection within a range of 4°–6°. Furthermore, by altering the filling medium of the test cavity, positioning the change value of SHWP can promote high-precision identification of hemoglobin concentrations of different blood types within the refractive index (RI) range of 1.6–1.7. The design of high-S multitask GEDD holds significant importance for expediting graphene material research. Moreover, it offers a novel approach for the precise application of SHW in the field of electromagnetic detection.**

***Index Terms*— Electromagnetic detection, ferroelectric crystal, graphene, second harmonic generation (SHG), strontium barium niobate (SBN).**

I. Introduction

IN THE realm of nonlinear optics [1], [2], second harmonic generation (SHG) [3] refers to the phenomenon where a light wave passing through a certain nonlinear optical material produces a new light wave with a frequency twice that of the input light [4]. Due to its advantages of frequency doubling, noninvasiveness, and high spatial resolution, SHG finds widespread applications in research areas such as nonlinear optics, material science, biomedical sciences, and spectroscopy [5], [6]. Ferroelectric crystals (FCs) [7] are a category of crystal materials with unique electrical properties. They exhibit a nonlinear electrical property called ferroelectricity, wherein the polarization direction within the crystal can be reversed under an external electric field, and this polarization is reversible. The nonlinear polarized response of FCs makes them excellent candidates for SHG. Common FCs include strontium barium niobate (SBN), lithium tantalate crystal (LTC), and potassium lithium sulfate [8]. Quasi-phase matching (QPM) [9] is a technique used to enhance nonlinear optical processes. It involves periodically altering the crystal's nonlinear properties, often achieved by creating FCs with periodically inverted polarity, to approximately satisfy the phase-matching conditions. By creating FCs with periodically inverted polarity, the efficiency of SHG can be significantly enhanced [10]. Fortunately, through the utilization of QPM technology and leveraging the spontaneous polarization and high nonlinear coefficient of SBN, Li et al. [11] achieved substantial enhancement of second harmonic wave (SHW) generation. Recently, Dumeige et al. [12] demonstrated that introducing FCs into photonic crystals can notably improve SHW generation through the photonic band gap (PBG) edge effect. Furthermore, researchers have proposed that graphene [13] or plasmas [14] can effectively enhance and modulate SHG, achieving promising outcomes through external light intensity or magnetic field adjustments. These studies present methods for enhancing SHG conversion efficiency.

Graphene's unique monolayer structure grants it high electron mobility, strong thermal conductivity, and weak absorption [15]. This makes graphene promising for a wide range of applications in electronic devices, conductive materials, sensors, biomedical applications, and more. Accurately identifying the number of graphene layers is essential for tailoring its properties, customization according to application needs, studying nanomaterials, and comprehending fundamental properties. Common methods for determining graphene layers include transmission electron microscopy (TEM) [16], Raman spectroscopy [17], and X-ray diffraction (XRD) [18]. However, they each have limitations. TEM can cause electron beam irradiation effects, resulting in sample damage or alteration. XRD is primarily used for analyzing 3-D materials and requires modifications and interpretations for graphene's 2-D identification. While Raman spectroscopy accurately analyzes graphene layers, its spatial resolution is limited, making it challenging to differentiate between single and double layers. Efficient and precise identification of graphene layers has

Manuscript received 20 October 2023; revised 13 December 2023; accepted 23 December 2023. Date of publication 8 January 2024; date of current version 2 July 2024. This work was supported by the College Student Innovation Training Program of the Nanjing University of Posts and Telecommunications. *(Corresponding author: Hai-Feng Zhang.)*

The authors are with the College of Electronic and Optical Engineering and the College of Flexible Electronics (Future Technology), Nanjing University of Posts and Telecommunications, Nanjing 210023, China (e-mail: hanlor@njupt.edu.cn).

This article has supplementary material provided by the authors and color versions of one or more figures available at https://doi.org/10.1109/TMTT.2023.3347528.

Digital Object Identifier 10.1109/TMTT.2023.3347528

TABLE I
PERFORMANCE OF GEDD

	Thickness detection	Angle detection	Bioelectromagnetic detection
Range	0.34~3.4 nm	4°~6°	1.6~1.7
S	62.1 GHz/nm	147 GHz/°	2.173 /RIU

become a research focus. Small-angle detection [19] offers high-precision measurements, eliminates visual distortion, and simplifies systems, finding potential applications in biology, optics, image processing, architecture, and civil engineering. Specifically, small-angle detection can be used for exploring 3-D structures of proteins and nucleic acids, correcting image distortions, and detecting structural deformations and damage in buildings and bridges [20]. Designing a high-precision, cost-effective angle detection device is a worthwhile research direction. Hemoglobin [21], an essential protein found in red blood cells, is responsible for transporting oxygen to various tissues and cells in the body. Measuring hemoglobin concentration provides crucial insights for health assessment, disease diagnosis, and treatment [22]. Babul and Stellwagen [23] proposed a method for measuring hemoglobin concentration using interferometric optics. In addition, Zafar et al. [24] proposed the possibility of detecting hemoglobin concentration based on plasma refractive index (RI). These traditional hemoglobin detection techniques suffer from low sensitivity (S) and time consumption, unable to meet real-time hemoglobin concentration monitoring demands. Therefore, the development of highly S, real-time bioelectromagnetic detection devices is essential.

In this article, the periodic layered structure achieved through the alternating arrangement of SBN and graphene, influenced by SHG, is referred to as a graphene electromagnetic detection device (GEDD) and is employed for various detection tasks. Utilizing the frequency shift f_1 of the SHW peak (SHWP), accurate identification of 1–10 layers of graphene (thickness ranging from 0.34 nm [25] to 3.4 nm) can be achieved under the condition $S = 62.1$ GHz/nm. Furthermore, utilizing the frequency shift f_2 of the SHWP, small-angle detections within the range of 4°–6° are feasible with S is 147 GHz/°. By filling the test cavity with hemoglobin of different blood types and determining the SHW conversion efficiency η, precise detection of hemoglobin concentration for three blood types can be accomplished through RI measurements. The integration of multiple tasks allows the proposed GEDD to circumvent the additional costs associated with the losses incurred by single-function detection devices. This approach also expands the research directions for GEDD. Table I illustrates the multifunctional, high-S, and compact nature of the GEDD introduced in this study, showcasing its potential for widespread application in biomedical and engineering detection scenarios.

II. STRUCTURAL DESIGN AND RESULTS

The schematic of the GEDD is illustrated in Fig. 1(a). The etching method for the layered structure can be referenced

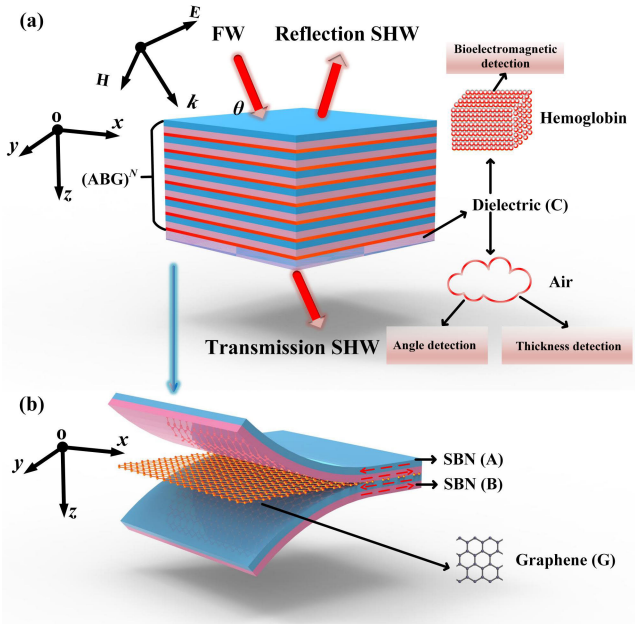

Fig. 1. Schematic of GEDD hierarchical structure. (a) Overall distribution of the structure is (ABG) ^{N}C, where C is the cavity to be tested, and different tasks are carried out when filling different media and (b) A and B are SBNs with different polarization directions, while G is graphene.

from the literature (details can be located in the Supplementary Material, Part 1) [26]. The periodic structure corresponding to GEDD is exposed to air (with an RI denoted as n_0) and operates at a temperature of 273 K. Since theoretical research is the focal point of this article, experimental validation is beyond the scope of this study. The SBN of periodic polarization is denoted as A and B, with the red dashed arrows in Fig. 1(b) indicating their opposing polarization directions. The graphene layer and the test cavity are represented as G and C, respectively. During graphene thickness and angle measurements, the test cavity is filled with air. For bioelectromagnetic detection purposes, test layer C is infused with hemoglobin of varying blood types for RI detection.

The thicknesses of the dielectric layers A, B, and C are $d_a = 3363.162$ nm, $d_b = 1904$ nm, and $d_c = 970$ nm, respectively. The monolayer graphene's thickness is $d_g = 0.34$ nm [27]. The second-order nonlinear coefficients of the respective dielectric layers are denoted as $\chi_a^{(2)}$, $\chi_b^{(2)}$, $\chi_c^{(2)}$, and $\chi_g^{(2)}$. The second-order nonlinear coefficient for the SBN layer is determined as $\chi^{(2)} = 27.2$ pm/V [28]. For the graphene layer (G) and the test layer (C), since they are not nonlinear media, their corresponding second-order nonlinear coefficients are 0. The refractive indices of SBN layers A and B under a fundamental wave (FW) and SHW are, respectively, denoted as $n_a^{(f)} = 1.617$, $n_a^{(s)} = 2.955$, $n_b^{(f)} = 1.68$, and $n_b^{(s)} = 3.245$ [29] (the modulation of the RI of the SBN layer can be found in Supplementary Materials, Part 2). The dielectric constant of the graphene layer is a function of its surface conductivity, which can be expressed as follows (Supplementary Material, Part 3, provides details on the modulation of graphene RI) [30]:

$$\varepsilon_g = 1 + i\frac{\sigma}{\varepsilon_0 \omega d_g} \tag{1}$$

where ε_0 represents the vacuum permittivity. The relationship between the RI of graphene and its dielectric constant can be expressed as $n_g = (\varepsilon_g)^{1/2}$. The conversion efficiency of the SHW is typically expressed as the ratio of light intensities [31]

$$\eta = \eta_t + \eta_r \tag{2}$$

where $\eta_t = I_t^{(s)+}/I_0^{(f)}$, $\eta_r = I_r^{(s)-}/I_0^{(f)}$, and $I_0^{(f)}$, $I_t^{(s)+}$, and $I_r^{(s)-}$ represent the incident light intensity of FW and the transmitted and reflected light intensities of SHW, respectively. The relationship between light intensity I and amplitude E can be expressed as [32]

$$E = (2I/n_0 c\varepsilon_0)^{1/2} \tag{3}$$

where c is the speed of light in a vacuum. In this article, multitask detection is achieved through the displacement and value of SHWP. The essence of finding SHWP lies in determining the efficiency of SHW conversion. Equation (3) indicates that solving for the output amplitudes of FW and SHW is crucial for determining the efficiency of SHW conversion. Thus, the expression for solving SHW output amplitude forms the basis for realizing multitask detection.

When FW propagates along the Z-axis within the graphene structure (details presented in Supplementary Material, Part 4), the electric field of FW in each layer can be represented as

$$E_t^{(f)} = E_t^{f+} e^{i\left[k_r^{(f)}(Z_t - Z_{t-1}) - \omega t\right]} + E_t^{f-} e^{-i\left[k_r^{(f)}(Z_t - Z_{t-1}) - \omega t\right]} \tag{4}$$

where "+" and "−" represent the transmitted and reflected waves of the FW, respectively. Here, $Z_0 = 0$ and $Z_t - Z_{t-1} = d_t$, where d_t stands for the thickness of the tth layer medium in the GEDD. $k_r^{(f)}$ denotes the wave vector in the r-layer medium, and it is determined by $k_r^{(f)} = n_r^{(f)} k_0^{(f)} \cos(\theta_r^{(f)})$, $\theta_r^{(f)} = \arcsin\left(n_0 \sin(\theta_0)/n_r^{(f)}\right)$, and $k_0^{(f)} = \omega/c$. Here, r represents layers A, B, C, and G, while n_0 stands for the RI of the air layer. According to the Voigt effect [33], it follows that $n_{rr}^{(f)} = k_r^{(f)}/(n_r^{(f)}\, n_r^{(f)})$. By employing the continuity conditions at the layer boundaries, define

$$\boldsymbol{D}_r = \begin{pmatrix} 1 & 1 \\ n_{rr}^{(f)} & -n_{rr}^{(f)} \end{pmatrix} \tag{5}$$

$$\boldsymbol{N}_r = \begin{pmatrix} \exp\left(ik_r^{(f)} d_t\right) & 0 \\ 0 & \exp\left(-ik_r^{(f)} d_t\right) \end{pmatrix}. \tag{6}$$

In this scenario, the total matrix of FW amplitudes can be represented as

$$\begin{pmatrix} E_T^{f+} \\ E_T^{f-} \end{pmatrix} = \boldsymbol{T}_F^f \begin{pmatrix} E_0^{f+} \\ E_0^{f-} \end{pmatrix}. \tag{7}$$

Defining $\boldsymbol{M}_1 = \boldsymbol{D}_g \boldsymbol{N}_g \boldsymbol{D}_g^{-1} \boldsymbol{D}_b \boldsymbol{N}_b \boldsymbol{D}_b^{-1} \boldsymbol{D}_a \boldsymbol{N}_a \boldsymbol{D}_a^{-1}$, the total matrix for the FW is expressed as

$$\boldsymbol{T}^f = \boldsymbol{D}_0^{-1} \boldsymbol{D}_c \boldsymbol{N}_c \boldsymbol{D}_c^{-1} \left(\boldsymbol{D}_g \boldsymbol{N}_g \boldsymbol{D}_g^{-1} \boldsymbol{D}_b \boldsymbol{N}_b \boldsymbol{D}_b^{-1} \boldsymbol{D}_a \boldsymbol{N}_a \boldsymbol{D}_a^{-1}\right)^N \boldsymbol{D}_0. \tag{8}$$

By determining the amplitude of the incident wave and utilizing $\boldsymbol{T}^f$, the reflection and transmission coefficients are obtained. Therefore, the amplitude of the electric field in each layer inside the structure can be solved (details can be seen in Supplementary Material, Part 5). Once the relative amplitudes within the multilayer structure are fully determined, the solution for the output amplitude of the SHW is considered. Within any layer of the graphene structure medium, the electric field of the SHW satisfies the following equation:

$$\partial^2 E_i^{(s)}(z)/\partial^2 z + k_{r(s)2} E_i^{(s)}(z) = -k_{0(s)2} \chi_i^{(2)} E_r^{(f)2}(z) \tag{9}$$

where "s" is used to denote the SHW. $k_r^{(s)}$ represents the SHW wave vector in the rth layer of the medium. $\boldsymbol{k}_r^{(s)} = n_r^{(s)} k_0^{(s)} \cos(\theta_r^{(s)})$, $\theta_r^{(s)} = \arcsin(n_0 \sin(\theta_0)/n_r^{(s)})$, and $k_0^{(s)} = 2\,\omega/c$. Defining $\boldsymbol{M}_2 = \boldsymbol{G}_g \boldsymbol{Q}_g \boldsymbol{G}_g^{-1} \boldsymbol{G}_b \boldsymbol{Q}_b \boldsymbol{G}_b^{-1} \boldsymbol{G}_a \boldsymbol{Q}_a \boldsymbol{G}_a^{-1}$, and $\boldsymbol{N}_1 = \boldsymbol{G}_g \boldsymbol{Q}_g \boldsymbol{G}_g^{-1} \boldsymbol{G}_b \boldsymbol{Q}_b \boldsymbol{G}_b^{-1}$, $\boldsymbol{N}_2 = \boldsymbol{G}_g\ \boldsymbol{Q}_g \boldsymbol{G}_g^{-1}$

$$\boldsymbol{G}_r = \begin{pmatrix} 1 & 1 \\ n_{rr}^{(s)} & -n_{rr}^{(s)} \end{pmatrix}; \quad \boldsymbol{B}_r = \begin{pmatrix} 1 & 1 \\ \frac{2n_{rr}^{(f)} k_0^{(f)}}{k_0^{(s)}} & -\frac{2n_{rr}^{(f)} k_0^{(f)}}{k_0^{(s)}} \end{pmatrix}$$

$$\boldsymbol{F}_r = \begin{pmatrix} \exp\left(2ik_r^{(f)} d_t\right) & 0 \\ 0 & \exp\left(-2ik_r^{(f)} d_t\right) \end{pmatrix}$$

$$\boldsymbol{Q}_r = \begin{pmatrix} \exp\left(ik_r^{(s)} d_t\right) & 0 \\ 0 & \exp\left(-ik_r^{(s)} d_t\right) \end{pmatrix}$$

$$A_r = \frac{-k_0^{(s)2} \chi_r^{(2)}}{k_r^{(s)2} - 4k_r^{(f)2}}; \quad C_r = \frac{-k_0^{(s)} \chi_r^{(2)}}{k_r^{(s)2}}.$$

The output amplitude of the SHW can be expressed as (details are explained in Supplementary Material, Part 6)

$$\begin{aligned}
\begin{pmatrix} E_N^{(s)+} \\ 0 \end{pmatrix} &= \boldsymbol{G}_0^{(-1)} \boldsymbol{G}_c \boldsymbol{Q}_c \boldsymbol{G}_c^{-1} \boldsymbol{M}_2^N \boldsymbol{G}_0 \begin{pmatrix} 0 \\ E_0^{(s)-} \end{pmatrix} \\
&+ \sum_{s=0}^{N} \boldsymbol{G}_0^{(-1)} \boldsymbol{G}_c \boldsymbol{Q}_c \boldsymbol{G}_c^{-1} \boldsymbol{M}_2^{N-s} \\
&\times \Bigg[(\boldsymbol{N}_1 \boldsymbol{B}_a \boldsymbol{F}_a - \boldsymbol{M}_2 \boldsymbol{B}_a) \begin{pmatrix} A_a \left(E_{3j-2}^{(f)+}\right)^2 \\ A_a \left(E_{3j-2}^{(f)-}\right)^2 \end{pmatrix} \\
&\quad + (\boldsymbol{N}_1 - \boldsymbol{M}_2) \begin{pmatrix} C_a \\ 0 \end{pmatrix} E_{3j-2}^{(f)+} E_{3j-2}^{(f)-} \\
&\quad + (\boldsymbol{N}_2 \boldsymbol{B}_b \boldsymbol{F}_b - \boldsymbol{N}_1 \boldsymbol{B}_b) \begin{pmatrix} A_b \left(E_{3j-1}^{(f)+}\right)^2 \\ A_b \left(E_{3j-1}^{(f)-}\right)^2 \end{pmatrix} \\
&\quad + (\boldsymbol{N}_2 - \boldsymbol{N}_1) \begin{pmatrix} C_b \\ 0 \end{pmatrix} E_{3s-1}^{(f)+} E_{3s-1}^{(f)-} \\
&\quad + \left(\boldsymbol{B}_g \boldsymbol{F}_g - \boldsymbol{N}_2 \boldsymbol{B}_g\right) \begin{pmatrix} A_g \left(E_{3j}^{(f)+}\right)^2 \\ A_g \left(E_{3j}^{(f)-}\right)^2 \end{pmatrix} \\
&\quad + (1 - \boldsymbol{N}_2) \begin{pmatrix} C_g \\ 0 \end{pmatrix} E_{3s}^{(f)+} E_{3s}^{(f)-} \Bigg] \\
&+ \left(\boldsymbol{B}_c \boldsymbol{F}_c - \boldsymbol{G}_c \boldsymbol{Q}_c \boldsymbol{G}_c^{-1} \boldsymbol{B}_c\right) \begin{pmatrix} A_c \left(E_{3N+1}^{(f)+}\right)^2 \\ A_c \left(E_{3N+1}^{(f)-}\right)^2 \end{pmatrix} \\
&+ \left(1 - \boldsymbol{G}_c \boldsymbol{Q}_c \boldsymbol{G}_c^{-1}\right) \begin{pmatrix} C_c \\ 0 \end{pmatrix} E_{3N+1}^{(f)+} E_{3N+1}^{(f)-}.
\end{aligned} \tag{10}$$

Through (8), the transmitted and reflected amplitudes of the SHW can be obtained. By utilizing the relationship between intensity and amplitude (3), the conversion efficiency of SHW can be deduced, rendering the SHWP usable within the GEDD. When the test cavity is no longer filled with air, the proposed GEDD is utilized for detecting physical quantities dependent on the RI. Therefore, the GEDD structure can be employed to measure the concentration of hemoglobin with different blood types and to identify specific blood types. Rakhshani and Mansouri-Birjandi [34] proposed a precise mathematical model to assess the RI of hemoglobin in different blood types (A, B, and O)

$$n(\lambda) = n_0 + \alpha C_{\mathrm{H}} + \beta T + \delta_1 \lambda + \delta_2 \lambda^2 + \delta_3 \lambda^3 \qquad (11)$$

where $n(\lambda)$ represents the wavelength-dependent RI and α, β, and δ are Cauchy coefficients with constant values specific to certain blood types. $\lambda = c/\omega$, where ω is the incident frequency. Apart from wavelength dependency, the RI of hemoglobin is also related to concentration C_{H} (in units of gram/liter) and temperature T (in units of kelvin).

III. Analysis and Discussion

The origin of the SHWP and the selection of the graphene chemical potential μ_c are crucial for the investigation. Let us first take the detection of a single graphene layer as an example, where $d_{\mathrm{gt}} = 0.34$ nm and $N = 30$. The incident optical intensity is determined as $I = 5.31$ mW/μm^2. The chemical potential μ_c is modulated by an external voltage (the regulation method for UC can be located in Part 7 of the Supplementary Materials) [35]. The significant enhancement in SHW conversion efficiency can be explained by the fact that the electromagnetic wave frequency is situated at the PBG, leading to an increase in electric field density and a reduction in the electromagnetic wave group velocity [31]. Consequently, the SHW output efficiency is greatly improved. This is further validated in Fig. 2. Fig. 2(a) and (b), respectively, shows the electromagnetic wave transmission spectra under FW and SHW states. In Fig. 2, the results depicted by the red dashed line were obtained using HFSS software, employing the finite element method. In comparison to the results obtained by the method presented in this article, the relative error in the boundary frequency points between the two is less than 0.01%. Taking into account the differences in precision and methodology, the results of both approaches are essentially consistent. The incident frequency for FW is $f = 353.144$ THz, and the SHW frequency is $f = 708.288$ THz. In Fig. 2(b), it resides at the transmission spectrum's bandgap edge [11]. The PBG effect can also be interpreted as a decrease in group velocity, prolonging the reaction time of electromagnetic waves with nonlinear media, thereby generating more SHWs.

Fig. 3 illustrates the relationship between the SHW conversion efficiency η and the FW frequency f. Six standard values of μ_c are given as 0.1, 0.3, 0.5, 0.7, 0.75, and 0.8 eV. As shown in Fig. 3(a), with an increase in μ_c, the SHWP (i.e., the peak value of η) gradually shifts to the left. Specifically, when the value of μ_c transitions from 0.8 to 0.75 eV, the corresponding

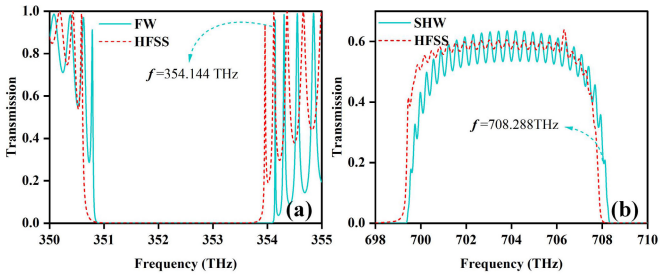

Fig. 2. Transmission curves for $\mu_c = 0.8$ eV with a normal incidence of electromagnetic waves. (a) FW. (b) SHW.

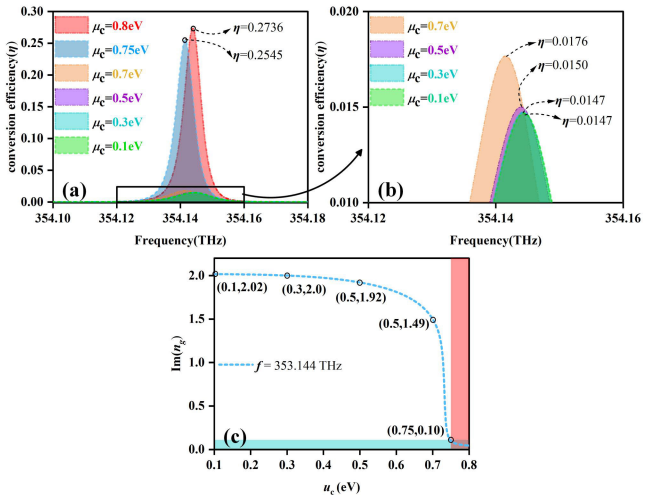

Fig. 3. When the incident angle μ_c changes and FW is incident in the forward direction, (a) comparative illustration of SHWP with varying graphene thickness, (b) enlarged view, and (c) imaginary part of the RI.

SHWP value decreases from 0.2736 to 0.2524. Furthermore, when μ_c decreases to 0.7 eV and below, the SHWP value drops below 0.02. As illustrated in Fig. 3(b), with the reduction of μ_c, the values of η decrease to 0.0176, 0.015, 0.0147, and 0.0147. To elucidate this phenomenon, Fig. 3(c) depicts the relationship curve between the imaginary part of the RI of graphene and the μ_c value. It is observed that when μ_c is less than 0.7 eV, the imaginary part of graphene exceeds 1. At this point, the substantial losses induced by graphene result in an exceedingly small η. Conversely, when μ_c is greater than 0.75 eV, the imaginary part sharply decreases to below 0.1, leading to a remarkable enhancement in SHWP. Pursuing maximal SHWP is a crucial requirement for achieving multitask detection, and thus, in the subsequent research, μ_c will be maintained at 0.8 eV.

Apart from nonlinear interactions, the enhancement of the internal electric field within the GEDD is also a contributing factor to the increase in SHW conversion efficiency. Figs. 4 and 5, respectively, illustrate the distribution of the internal electric field for FW and SHW incidences. Here, we assume an incident optical intensity of 1 V/m for the electromagnetic wave. It has been observed that the FW generates two distinct electric field peaks within the GEDD. These peaks exceed 200 V/m. This phenomenon can be attributed to the unique resonant effects of the photonic crystal [28], resulting in intense reflection and scattering of

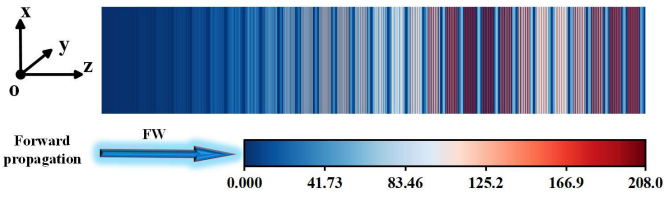

Fig. 4. Electric field distribution of FW within the GEDD.

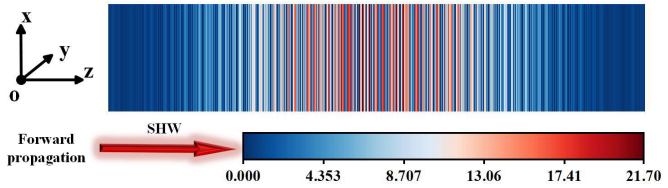

Fig. 5. Electric field distribution of SHW within the GEDD.

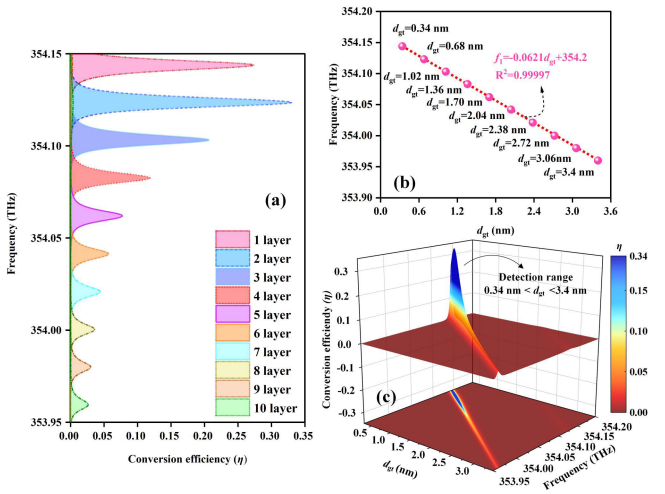

Fig. 6. Schematic representation of thickness detection. (a) Relationship curve between conversion efficiency η and FW incident frequency under the case of different thickness conditions, (b) detection performance of FW incident frequency f_1 concerning graphene thickness d_{gt}, and (c) variation of values η with d_{gt} continuous changes within a certain frequency range.

the FW within the structure. This enhances the electric field intensity and extends the interaction time with the nonlinear medium [29].

The FW is influenced by the scattering and interference effects of the periodic structure, ultimately leading to the constructive growth of SHW within the structure. As depicted in Fig. 5, when SHW is incident within the GEDD, the electric field strength continuously increases, eventually exceeding 20 V/m. The exceptionally high electric field mode density of FW is a crucial factor in enhancing the SHWP [29], enabling the possibility of multitask detection using the SHWP.

Similar to the shift of the peak efficiency frequency due to changes in μ_c, the change in the number of graphene layers, referred to as d_{gt}, will alter the transmittance curve of electromagnetic waves within the structure. This, in turn, will impact the PBG boundary effects and the strength of the electric field within the GEDD, consequently altering the values of η. As depicted in Fig. 6(a), variation in d_{gt} results in the movement of the SHWP within a specific frequency range. As the number of graphene layers increases from 1 to 10 (d_{gt} changes to 0.34, 0.68, 1.02, 1.36, 1.7, 2.04, 2.38, 2.72, 3.06, and 3.4 nm), the corresponding frequency f_1 of the SHWP shifts from 353.144 to 353.960 THz. The consistent η values above 0.01 indicate significant responsiveness in the detection process. To accurately measure the thickness propagation ability of the GEDD, Fig. 6(b) considers ten monitoring points between 0.34 and 3.4 nm, spaced by 0.34-nm increments. Employing the linear fitting technique (LFT) on the detection data yields the LFT equation: $f_1 = -0.0621\ d_{gt} + 354.2$. The slope S is 62.1 GHz/nm, signifying the high responsiveness of the GEDD structure to changes in graphene thickness. A thickness alteration of 1 nm can be monitored through a peak shift of the SHWP by 62.1 GHz, enabling the conversion of nanometer-scale graphene thickness changes into a sensitive response at the gigahertz level. Furthermore, the fitting coefficient $R^2 = 0.99997$ demonstrates a robust linear relationship in the LFT equation. Fig. 6(c) illustrates the variation in SHWP as d_{gt} ranges from 0.34 to 3.0 nm. Within this range, the highest value of η is 0.34, gradually decreasing with the increase in d_{gt}. Correspondingly, f_1 also shifts in the direction of decrease. This indicates the potential to detect changes in graphene thickness through the movement of SHWP within a specific frequency range, holding significance for future research in graphene detection.

When conducting angle detection, as shown in Fig. 1, graphene thickness inside the cavity is maintained as a monolayer ($d_{gt} = 0.34$ nm), and the cavity for the test layer is still filled with air. By locking the peak shift of the SHWP at frequency f_2, the proposed GEDD enables precise angle detection. Fig. 7(a) presents the corresponding values of η under various incident angle conditions. When θ changes to 4°, 4.5°, 5°, 5.5°, and 6°, the corresponding f_2 changes from 354.38 to 354.674 THz. The LFT equation in Fig. 7(b) is $f_2 = 0.147\theta + 353.8$. The slope $S = 147$ GHz/°, indicating that every 1° change in the angle can be detected by shifting the frequency point by 147 GHz. In addition, the coefficient R^2, used to evaluate the quality of LFT, is 0.9966, demonstrating the good linearity of the LFT equation [30]. Fig. 7(c) illustrates the variation curve of the corresponding SHWP from 353.2 to 354.7 THz as the angle changes from 3° to 6° in increments of 0.001°. The highest η value reaches 0.41. As the SHWP shifts, an increase in the angle gradually reduces the η value. The relationship between the angle and the frequency f_2 indicates the feasibility of performing small-angle detection within a certain range. The high-S of f_2 stems from its nonlinear optical characteristics; specifically, the SHW signal is directly proportional to the square of the incident light intensity. This enables effective response and measurement of subtle angular changes, making it of crucial significance in optical image processing and architectural engineering.

The limited angular detection range is directly attributed to the high dependence on phase matching between the FW and SHW, coupled with a unique structural design [29].

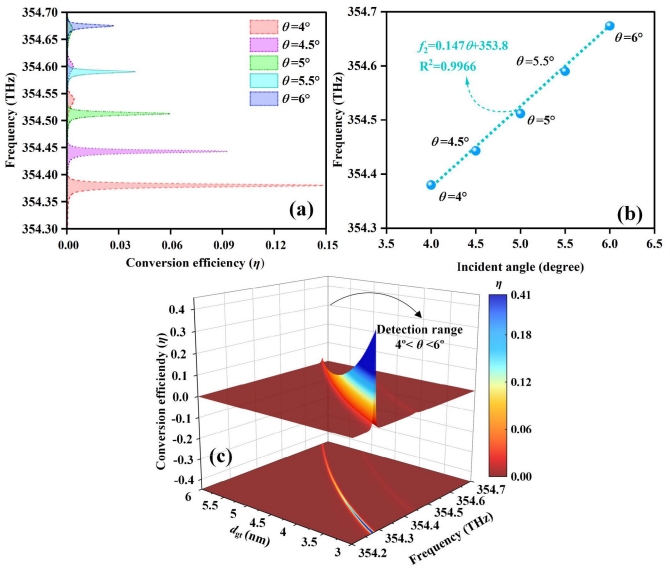

Fig. 7. Schematic representation of angle detection. (a) Relationship curves between the values of η and incident frequency f_2 under the case of different angle conditions. (b) Detection performance of FW incident frequency f_2 concerning incident angle θ. (c) Variation of the values η influenced by θ within a continuous range.

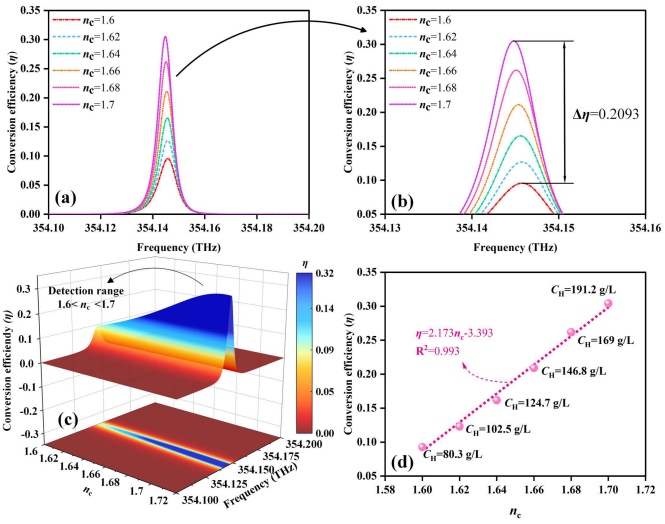

Fig. 8. Schematic representation of biometric detection. (a) Relationship curve between hemoglobin RI n_c and η. (b) Magnified image. (c) Continuous variation of SHWP influenced by n_c. (d) Detection performance of the values of η variation concerning hemoglobin n_c.

TABLE II
SUMMARY OF MODEL COEFFICIENTS [34]

Parameter	unit	Blood type A	Blood type B	Blood type O
n_0	RIU^{-1}	1.54712	1.54712	1.54712
α	L/g	9.014×10^{-4}	11.09×10^{-4}	11.26×10^{-4}
β	1°/K	-6.497×10^{-5}	-6.497×10^{-5}	-6.497×10^{-5}
δ_1	nm^{-1}	-8.47×10^{-6}	-8.47×10^{-6}	-8.47×10^{-6}
δ_2	nm^{-2}	7.08×10^{-7}	8.014×10^{-7}	7.742×10^{-7}
δ_3	nm^{-3}	-1.28×10^{-10}	-2.286×10^{-10}	-1.823×10^{-10}

Expanding the angular detection range can be achieved by innovatively designing structures to reduce the S-to-phase matching. This approach aims to mitigate the impact of conversion efficiency, thereby enabling a broader scope for angular detection.

In this study, the precise technique involving hollow submicrometer-sized micropipettes based on micro-perfusion technology is employed to perform RI detection of the hemoglobin under test [36]. The hemoglobin under examination is injected into the test cavity using the micropipettes, and the accurate technique is highlighted. Table II presents the relevant parameters of the hemoglobin RI expression under different blood type conditions. Rakhshani and Mansouri-Birjandi [34] conducted experimental curve fitting based on previous research and obtained the input data displayed in Table II. When the incident wavelength and environmental temperature are determined, the RI of hemoglobin is solely correlated to its concentration C_H.

The hemoglobin under test is injected into the test cavity. By locking the value of SHWP, the proposed GEDD can accurately detect hemoglobin concentration and distinguish blood types. Fig. 8(a) shows the SHWP of different hemoglobin concentrations (n_c = 1.6, 1.62, 1.64, 1.66, 1.68, and 1.7). The magnified image is shown in Fig. 8(b). As n_c increases, SHWP gradually rises and shifts slightly to the right. The peak values of SHWP are 0.0928, 0.1230, 0.1617, 0.2091, 0.2618, and 0.3042. The difference between the highest peak and the lowest peak of SHWP is η = 0.2093. Fig. 8(c) illustrates the continuous variation of SHWP as n_c changes within the range of 1.6–1.7, in the frequency range of 354.1–354.2 THz. Within the detection range, η values remain above 0.1. SHWP is situated around 353.75 THz and the growth rate significantly slows down after n_c = 1.7, thus establishing the detection range as 1.6–1.7. It is noteworthy that the detection range can be expanded by sacrificing sensitivity, achieved through the reduction of the thickness of the sensing layer. By locking the growth of SHWP, the GEDD can achieve high-precision hemoglobin concentration detection within a certain range. Taking the example of blood type A's hemoglobin concentration in Fig. 8(d), within the range of 1.6–1.7, detection points are collected at intervals of 0.2, corresponding to hemoglobin concentrations C_H of 80.3, 102.5, 124.7, 146.8, and 191.2 g/L. The LFT equation is $\eta = 2.173\ n_c - 3.393$, with S = 2.173 /RIU and R^2 = 0.993, indicating high-S and reliability in GEDD detection. Hemoglobin concentrations are typically 100–135 g/L for children and 120–170 g/L for adults [24]. In Fig. 8(d), the measurement range for blood type A hemoglobin is 80.3–191.2 g/L, achieving full coverage.

In addition to accurately identifying hemoglobin concentration, SHWP can also differentiate between different blood types. Fig. 9 depicts the relationship between hemoglobin concentration C_H and its corresponding n_c for the blood types A, B, and O. Given the detection range of 1.6–1.7, a specific region is selected for the A, B, and O hemoglobin concentration detection, indicated by the light blue area. The light blue area indicates the concentration range within which

TABLE III
PUBLISHED REPORTS COMPARED WITH THE PROPOSED GEDD IN TERMS OF PERFORMANCE

Refs.	SHW	Multitasking	Detection physical quantities	Detection performance	
[37]	×	×	Angle detection	Range	25°~70°
				S	0.5 THz/°
[38]	×	×	Angle detection	Range	5°~45°
				S	28 MHz/°
[27]	×	×	Graphene layers number	Range	1~8 layers
				S	×
[39]	×	×	Graphene layers number	Range	1-5 layers
				S	×
[24]	×	×	Detecting hemoglobin concentration	Range	1~1.03 RIU^{-1}
				S	1100 nm/RIU
[40]	√	×	RI detection	Range	1.33 ~ 1.39 RIU^{-1}
				S	×
[41]	√	×	PH detection	Range	0 ~ 14
				S	×
This article	√	√	Graphene layers number	Range	1~10 layers
				S	62.1GHz/nm
			Angle detection	Range	4°~6°
				S	147 GHz/°
			Bioelectromagnetic detection	Range	1.6~1.7 RIU^{-1}
				S	2.173 /RIU

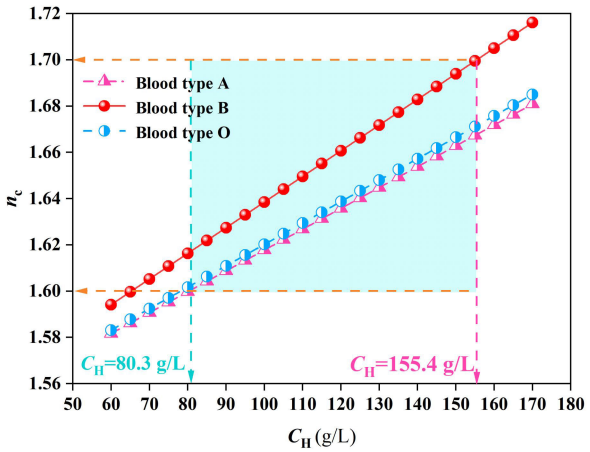

Fig. 9. Scatter plot of the relationship between hemoglobin concentration C_H and its n_c in different blood types. Here, the temperature T is 273 K, and the incident wave frequency is 354.144 THz.

A, B, and O hemoglobin can be measured simultaneously. In this case, the lower limit of measurement is determined by type A hemoglobin, with a concentration of $C_H = 80.3$ g/L, and the upper limit of measurement is determined by type B hemoglobin, with a concentration of $C_H = 155.4$ g/L. The final detection range spans from 80.3 to 155.4 g/L, enabling concentration detection for hemoglobin of different blood types within this range.

IV. PERFORMANCE COMPARISON

To systematically and intuitively showcase the benefits of the proposed GEDD, we have compiled Table III, which catalogs a selection of previously reported detection devices known for their exceptional performance. Through this comparative analysis, it becomes evident that the GEDD presented in this correspondence embodies a fusion of SHW and multitasking detection capabilities, outperforming its predecessors in several aspects. In particular, compared with existing SHW detection methods, our RI detection approach covers a broader range, incorporating angular and thickness measurements that are uncommon in existing studies. Consequently, the investigation into this GEDD and SHG, as detailed within this article, unveils distinct advancements and holds substantial value.

V. CONCLUSION

In conclusion, an SHG-based GEDD is introduced in this article, which enables graphene thickness detection, angle detection, and hemoglobin RI detection under a forward incident scale. In comparison with previously proposed detection devices, the proposed GEDD demonstrates more innovation and breakthroughs. The integration of multiple functions allows the GEDD to simultaneously perform the tasks of several single-function detection devices. Adjusting structural parameters and incident light intensity can optimize the phase difference between FW and SHW, and the PBG edge effect significantly enhances the conversion efficiency of SHW. The higher SHWP serves as the foundation for multitask detection. By locking the frequency shift f_1 of SHWP within a frequency range, accurate detection of graphene layers (1–10 layers) can be achieved, corresponding to $S = 62.1$ GHz/nm. Amplifying graphene's nanometer-level change to gigahertz-level detection enhances accuracy. Altering the incident angle allows locking the frequency shift f_2 of SHWP for angle detection, with an angle detection range of 4°–6°. With high-S ($S = 147$ GHz/°), small-angle detection finds crucial

applications in bridge construction and biometric image recognition. Changing the detected layer to include hemoglobin of different blood types enables precise detection of hemoglobin concentration within the range of 1.6–1.7 (the covered hemoglobin concentrations ranged from 80.3 to 155.4 g/L, with an S value of 2.173/RIU). The given GEDD features high sensitivity and multitask processing capabilities, promising applications in industrial settings, construction surveying, biomedical sciences, and beyond.

REFERENCES

[1] W. T. Buono and A. Forbes, "Nonlinear optics with structured light," *Opto-Electron. Adv.*, vol. 5, no. 6, pp. 210174-1–210174-19, Jun. 2022.

[2] Y. Li, J. Luo, and S. Zhao, "Local polarity-induced assembly of second-order nonlinear optical materials," *Accounts Chem. Res.*, vol. 55, no. 23, pp. 3460–3469, Nov. 2022.

[3] J. Enomoto, R. Ishikawa, and K. Honjo, "Second harmonic treatment technique for bandwidth enhancement of GaN HEMT amplifier with harmonic reactive terminations," *IEEE Trans. Microw. Theory Techn.*, vol. 65, no. 12, pp. 4947–4952, Dec. 2017.

[4] S. Yamada et al., "Second-harmonic generation in a silicon-carbide-based photonic crystal nanocavity," *Opt. Lett.*, vol. 39, no. 7, pp. 1768–1771, Mar. 2014.

[5] S. Buckley et al., "Second-harmonic generation in GaAs photonic crystal cavities in (111)B and (001) crystal orientations," *ACS Photon.*, vol. 1, no. 6, pp. 516–523, May 2014.

[6] K. S. Champlin and D. R. Singh, "Small-signal second-harmonic generation by a nonlinear transmission line (short paper)," *IEEE Trans. Microw. Theory Techn.*, vol. MTT-34, no. 3, pp. 351–353, Mar. 1986.

[7] C. Qiu et al., "Transparent ferroelectric crystals with ultrahigh piezoelectricity," *Nature*, vol. 577, no. 7790, pp. 350–354, Jan. 2020.

[8] V. Van and S. K. Chaudhuri, "A hybrid implicit-explicit FDTD scheme for nonlinear optical waveguide modeling," *IEEE Trans. Microw. Theory Techn.*, vol. 47, no. 5, pp. 540–545, May 1999.

[9] A. Bahabad, M. M. Murnane, and H. C. Kapteyn, "Quasi-phase-matching of momentum and energy in nonlinear optical processes," *Nature Photon.*, vol. 4, no. 8, pp. 570–575, Jun. 2010.

[10] S. A. Denev, T. T. A. Lummen, E. Barnes, A. Kumar, and V. Gopalan, "Probing ferroelectrics using optical second harmonic generation," *J. Amer. Ceram. Soc.*, vol. 94, no. 9, pp. 2699–2727, Aug. 2011.

[11] J. Li, Z. Li, Y. Sheng, and D. Zhang, "Giant enhancement of second harmonic generation in poled ferroelectric crystals," *Appl. Phys. Lett.*, vol. 91, no. 2, pp. 1599–1604, Jul. 2007.

[12] Y. Dumeige et al., "Enhancement of second-harmonic generation in a one-dimensional semiconductor photonic band gap," *Appl. Phys. Lett.*, vol. 78, no. 20, pp. 3021–3023, May 2001.

[13] A. Majumdar, J. Kim, J. Vuckovic, and F. Wang, "Electrical control of silicon photonic crystal cavity by graphene," *Nano Lett.*, vol. 13, no. 2, pp. 515–518, Jan. 2013.

[14] B. Wang and M. A. Cappelli, "A plasma photonic crystal bandgap device," *Appl. Phys. Lett.*, vol. 108, no. 16, Apr. 2016, Art. no. 161101.

[15] X. Gan et al., "Strong enhancement of light-matter interaction in graphene coupled to a photonic crystal nanocavity," *Nano Lett.*, vol. 12, no. 11, pp. 5626–5631, Oct. 2012.

[16] A. W. Robertson and J. H. Warner, "Atomic resolution imaging of graphene by transmission electron microscopy," *Nanoscale*, vol. 5, no. 10, pp. 4079–4093, 2013.

[17] L. M. Malard, M. A. Pimenta, G. Dresselhaus, and M. S. Dresselhaus, "Raman spectroscopy in graphene," *Phys. Rep.*, vol. 473, no. 5, pp. 51–87, 2009.

[18] T. N. Blanton and D. Majumdar, "Characterization of X-ray irradiated graphene oxide coatings using X-ray diffraction, X-ray photoelectron spectroscopy, and atomic force microscopy," *Powder Diffraction*, vol. 28, no. 2, pp. 68–71, Apr. 2013.

[19] B. Zhu, Q. Fu, K. Chen, and J. Ge, "Liquid photonic crystals for mesopore detection," *Angew. Chem.*, vol. 130, no. 1, pp. 258–262, Jan. 2018.

[20] J. Villatoro, V. P. Minkovich, and J. Zubia, "Photonic crystal fiber interferometric vector bending sensor," *Opt. Lett.*, vol. 40, no. 13, p. 3113, Jun. 2015.

[21] A. K. Sharma, "Plasmonic biosensor for detection of hemoglobin concentration in human blood: Design considerations," *J. Appl. Phys.*, vol. 114, no. 4, Jul. 2013, Art. no. 044701.

[22] A. K. Sharma and J. Gupta, "Graphene based chalcogenide fiber-optic evanescent wave sensor for detection of hemoglobin in human blood," *Opt. Fiber Technol.*, vol. 41, pp. 125–130, Mar. 2018.

[23] J. Babul and E. Stellwagen, "Measurement of protein concentration with interferences optics," *Anal. Biochemistry*, vol. 28, pp. 216–221, Jul. 1969.

[24] R. Zafar, S. Nawaz, G. Singh, A. d'Alessandro, and M. Salim, "Plasmonics-based refractive index sensor for detection of hemoglobin concentration," *IEEE Sensors J.*, vol. 18, no. 11, pp. 4372–4377, Jun. 2018.

[25] Z. H. Ni et al., "Graphene thickness determination using reflection and contrast spectroscopy," *Nano Lett.*, vol. 7, no. 9, pp. 2758–2763, Jul. 2007.

[26] L. Qi, C. Liu, and S. M. A. Shah, "A broad dual-band switchable graphene-based terahertz metamaterial absorber," *Carbon*, vol. 153, pp. 179–188, Nov. 2019.

[27] X. Zhou, X. Ling, H. Luo, and S. Wen, "Identifying graphene layers via spin Hall effect of light," *Appl. Phys. Lett.*, vol. 101, no. 25, Dec. 2012, Art. no. 251602.

[28] S. M. Kostritskii, P. Bourson, M. Aillerie, M. D. Fontana, and D. Kip, "Quantitative evaluation of the electro-optic effect and second-order optical nonlinearity of lithium tantalate crystals of different compositions using Raman and infrared spectroscopy," *Appl. Phys. B, Lasers Opt.*, vol. 82, no. 3, pp. 423–430, Mar. 2006.

[29] J.-J. Li, Z.-Y. Li, and D.-Z. Zhang, "Second harmonic generation in one-dimensional nonlinear photonic crystals solved by the transfer matrix method," *Phys. Rev. E, Stat. Phys. Plasmas Fluids Relat. Interdiscip. Top.*, vol. 75, no. 5, May 2007.

[30] J.-Y. Sui, J.-H. Zou, S.-Y. Liao, B.-X. Li, and H.-F. Zhang, "High sensitivity multiscale and multitasking terahertz Janus sensor based on photonic spin Hall effect," *Appl. Phys. Lett.*, vol. 122, no. 23, Jun. 2023, Art. no. 231105.

[31] C. Yang, C. Guo, C. Peng, and H. Zhang, "Second harmonic generation in 1D nonlinear plasma photonic crystals," *Annalen der Physik*, vol. 535, no. 9, Jul. 2023, Art. no. 2300190.

[32] S. Rao, J. Zhang, B. Wan, and H. Zhang, "Theoretical investigation of the nonreciprocal bistable absorption of electromagnetic waves in one-dimensional photonic crystals combined with the nonlinear magnetized plasma defect layer," *Waves Random Complex Media*, vol. 22, pp. 1–21, Sep. 2022.

[33] R. Carey and B. W. J. Thomas, "The theory of the Voigt effect in ferromagnetic materials," *J. Phys. D, Appl. Phys.*, vol. 7, no. 17, pp. 2362–2368, Nov. 1974.

[34] M. R. Rakhshani and M. A. Mansouri-Birjandi, "High sensitivity plasmonic refractive index sensing and its application for human blood group identification," *Sens. Actuators B, Chem.*, vol. 249, pp. 168–176, Oct. 2017.

[35] O. Hosten and P. Kwiat, "Observation of the spin Hall effect of light via weak measurements," *Science*, vol. 319, no. 5864, pp. 787–790, Feb. 2008.

[36] F. Intonti et al., "Rewritable photonic circuits," *Appl. Phys. Lett.*, vol. 89, no. 21, Nov. 2006, Art. no. 211117.

[37] B.-F. Wan, Z.-W. Zhou, Y. Xu, and H.-F. Zhang, "A theoretical proposal for a refractive index and angle sensor based on one-dimensional photonic crystals," *IEEE Sensors J.*, vol. 21, no. 1, pp. 331–338, Jan. 2021.

[38] A. M. Gargari et al., "A wireless metamaterial-inspired passive rotation sensor with submilliradian resolution," *IEEE Sensors J.*, vol. 18, no. 11, pp. 4482–4490, Jun. 2018.

[39] C. Mi et al., "Precise identification of graphene layers at the air-prism interface via a pseudo-Brewster angle," *Opt. Lett.*, vol. 42, no. 20, pp. 4135–4138, Oct. 2017.

[40] M. S. Verma and M. Chandra, "Second harmonic generation-based nonlinear plasmonic RI-sensing in solution: The pivotal role of the particle size," *Phys. Chem. Chem. Phys.*, vol. 23, no. 45, pp. 25565–25571, Nov. 2021.

[41] A. Khorsandi, S. Shojaei, and F. Hosseinibalam, "Second-harmonic laser-coupled optical fiber sensor for pH measurement and corrosion detection based on evanescent field absorption," *Opt. Laser Technol.*, vol. 44, no. 5, pp. 1564–1569, Jul. 2012.

Cheng Yang was born in Guizhou, China, in 2003. He is currently pursuing the bachelor's degree at the College of Electronic and Optical Engineering and the College of Flexible Electronics (Future Technology), Nanjing University of Posts and Telecommunications, Nanjing, China.

His main research interests include second harmonic generation, graphene photonic crystal, and electromagnetic detection.

Chu-Ming Guo was born in Jiangsu, China, in 2003. He is currently pursuing the bachelor's degree at the College of Electronic and Optical Engineering and the College of Flexible Electronics (Future Technology), Nanjing University of Posts and Telecommunications, Nanjing, China.

His main research interests include nonlinear photonic crystals, second harmonic generation, and second harmonic applications.

Jie Xu was born in Nanjing, China, in 2003. He is currently pursuing the bachelor's degree at the College of Electronic and Optical Engineering and the College of Flexible Electronics (Future Technology), Nanjing University of Posts and Telecommunications, Nanjing, China.

His main research interests include the photonic crystal sensor and optimization algorithm.

Hai-Feng Zhang was born in Jiangxi, China, in 1978. He received the Ph.D. degree from the College of Electronic and Information Engineering, Nanjing University of Aeronautics and Astronautics, Nanjing, China, in 2014.

He is currently working as a Professor at the College of Electronic and Optical Engineering and the College of Flexible Electronics (Future Technology), Nanjing University of Posts and Telecommunications, Nanjing. His main research interests include computational electromagnetics, graphene photonic crystal, plasma stealthy, and electromagnetic properties of metamaterials and metastructure.